JACS
JOURNAL OF THE AMERICAN CHEMICAL SOCIETY

Article

pubs.acs.org/JACS

Colloidal Synthesis of 1T-WS_2 and 2H-WS_2 Nanosheets: Applications for Photocatalytic Hydrogen Evolution

Benoit Mahler, Veronika Hoepfner, Kristine Liao, and Geoffrey A. Ozin*

Materials Chemistry and Nanochemistry Research Group, Department of Chemistry, University of Toronto, 80 St. George Street, Toronto, Ontario Canada M5S 3H6

Supporting Information

ABSTRACT: In recent years, a lot of attention has been devoted to monolayer materials, in particular to transition-metal dichalcogenides (TMDCs). While their growth on a substrate and their exfoliation are well developed, the colloidal synthesis of monolayers in solution remains challenging. This paper describes the development of synthetic protocols for producing colloidal WS_2 monolayers, presenting not only the usual semiconducting prismatic 2H-WS_2 structure but also the less common distorted octahedral 1T-WS_2 structure, which exhibits metallic behavior. Modifications of the synthesis method allow for control over the crystal phase, enabling the formation of either 1T-WS_2 or 2H-WS_2 nanostructures. We study the factors influencing the formation of the two WS_2 nanostructures, using X-ray diffraction, microscopy, and spectroscopy analytical tools to characterize them. Finally, we investigate the integration of these two WS_2 nanostructured polymorphs into an efficient photocatalytic hydrogen evolution system to compare their behavior.

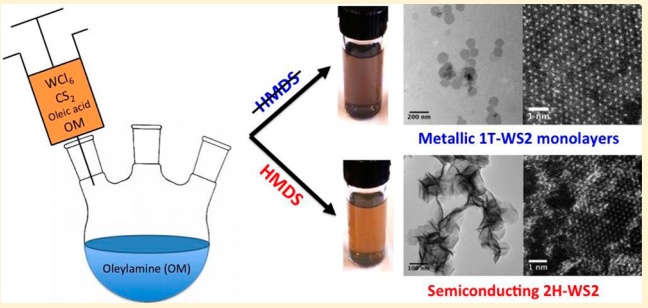

INTRODUCTION

The discovery of graphene and the development of different physical and chemical methods with which to synthesize it[1−4] has ignited global interest in the study of various types of monolayered materials. Among the numerous kinds of materials that have the capacity to form monolayers,[5,6] much attention has been devoted to the lamellar transition-metal dichalcogenides (TMDC).[7] This class of materials—in which a monolayer is comprised of two close-packed chalcogenide planes sandwiching a transition-metal layer—exhibits numerous interesting properties, ranging from insulators to semiconductors to metals,[8] and could find applications in diverse fields such as catalysis,[9] photovoltaics,[10,11] optoelectronics,[12,13] and spintronics.[14]

In this field one can distinguish three ways of preparing monolayer TMDCs: (a) exfoliation, (b) substrate growth, and (c) colloidal synthesis. The exfoliation method can be purely physical (i.e., "tape" method),[1,15] chemically assisted (e.g., by sonication in a good solvent such as NMP),[16] or purely chemical through intercalation (with lithium for example).[17,18] Exfoliation methods allow for the preparation of large amounts of monolayers (especially via chemical exfoliation) but generally lead to a polydispersed distribution of flakes without any control over their size, shape, or nature of their edges. The second approach—the substrate growth method—creates large monolayers[19] with high crystallinity and control over shapes[20] and edges but is intrinsically limited by the amount of monolayers being produced. Third, the colloidal chemical synthesis strategy can in principle enable the preparation of large batches of TMDCs monolayers with good crystallinity, monodispersity, and control over the edges. However, it is quite underdeveloped compared to the two other preparation schemes and only a few examples are known.[21−24]

Among monolayer TMDCs, tungsten disulfide (WS_2) is of particular interest as its electronic band gap undergoes an indirect (1.4 eV) to direct (2 eV) transition when its size is reduced from bulk to monolayer.[8] In monolayer form, WS_2 nanosheets can find numerous applications ranging from fluorescent emitters[25] and field effect transistors[26] to photovoltaics[10] and photocatalysis.[27] However, to the best of our knowledge only a few reports of colloidal syntheses exist,[21,22] and they rarely mention the optical properties of the synthesized nanosheets.

Until recently, most of the attention has been focused on semiconducting WS_2 and MoS_2 monolayers, both of which possess a prismatic coordination for the metal atom (2H structure). This type of structure is generally produced by physical exfoliation or vapor growth methods. By using the lithium exfoliation technique, it is possible to obtain a different structure with an octahedral coordination (1T structure) for the metal atom. The 1T structure exhibits metallic properties.[28] These 1T-WS_2 and 1T-MoS_2 monolayers have been recently shown to be very efficient hydrogen evolution electrocatalysts.[29−32]

Received: June 22, 2014
Published: September 15, 2014

   dx.doi.org/10.1021/ja506261t | J. Am. Chem. Soc. 2014, 136, 14121−14127

MoS_2 and WS_2 can also act as efficient earth-abundant cocatalysts[33] for photocatalytic hydrogen evolution. Recently, exfoliated 1T-MoS_2 monolayers have also been used as a cocatalyst in a silicon-based photoelectrochemical cell for hydrogen evolution.[34]

In this study, we first describe a novel colloidal synthesis method for colloidally stable WS_2 monolayers. Surprisingly, this method does not produce the expected semiconducting prismatic 2H-WS_2 structure. Instead, it creates metallic WS_2 nanosheets possessing a distorted octahedral 1T-WS_2 structure. A slight modification of this synthesis leads to the formation of aggregated 2H-WS_2 nanostructures. We then explore the different structures and properties of these nanosheets using electron microscopy, optical spectroscopy, X-ray photoelectron spectroscopy (XPS), and powder X-ray diffraction (PXRD). These results highlight the characterization techniques deemed suitable to probe the synthetic mechanisms leading to the two different crystal structures: distorted 1T-WS_2 and regular 2H-WS_2. Finally, we investigate the photocatalytic water splitting properties of the two different structures by preparing a nanocomposite TiO_2-WS_2, which is found to exhibit high H_2 evolution rates in the case of the distorted 1T-WS_2 nanostructure relative to the regular 2H-WS_2 form. The origin of these differences is discussed.

EXPERIMENTAL SECTION

Materials. Oleylamine (technical, 70%, Aldrich), tungsten hexachloride (WCl_6, 99.9%, Aldrich), oleic acid (90%, Aldrich), carbon disulfide (CS_2, anhydrous, 99%, Sigma-Aldrich), hexamethyldisilazane (99.9%, Aldrich), hexane (ACS grade, 98.5%, Caledon), and isopropanol (99.5%, EMD) are used as received without purification.

Representative Synthesis of 1T-WS_2 Nanosheets. In a 100 mL three-neck flask, 15 mL of oleylamine is degassed for 1 h under vacuum at 65 °C. The oleylamine is then heated up to 320 °C under argon atmosphere. Meanwhile, 50 mg of WCl_6 (0.125 mmol) and 300 μL of oleic acid are mixed in a vial and sonicated until full dissolution. The solution changes color from dark blue to dark brown during the WCl_6 dissolution process. The vial is then flushed with nitrogen, and 5 mL of oleylamine is added. This induces a second color change from dark brown to light yellow. Prior to injection, 240 μL of CS_2 is swiftly introduced, inducing a temperature increase and a further color change to orange. The solution immediately begins to thicken and solidify over time. This precursor mixture is injected dropwise into the hot oleylamine solution over a 30 min interval using a syringe pump. After injection, the reaction mixture is left to cool down to room temperature. The WS_2 nanosheets are then precipitated by adding 15 mL of hexane and 15 mL of isopropanol followed by centrifugation. The nanosheets are finally redispersed in 10 mL of hexane.

Representative Synthesis of 2H-WS_2 Nanosheets. Introducing 500 μL of hexamethyldisilazane (HMDS) into the oleylamine after the degassing step and prior to injection induces the formation of 2H-WS_2 nanosheets instead of the 1T-WS_2 nanostructure. The nanosheets are partially aggregated and form a flower-like morphology.

Preparation of the TiO_2-WS_2 Nanocomposite. In an agate mortar, 50 mg of TiO_2 nanopowder (P25, Degussa) and 385 μL of a WS_2 dispersion in hexane (1.3 mg mL^{-1}) are ground together until dry. The solid is then dispersed by the addition of 1 mL ethanol and ground again. The composite powder is dried overnight in an oven at 80 °C.

Characterization Methods. *TEM.* Low-magnification transmission electron microscopy (TEM) images were acquired using a Hitachi 7000 TEM with a LaB_6 filament operating at 100 kV. The high-angle annular dark-field (HAADF) high-resolution scanning electron microscopy (HRSTEM) images were taken using a FEI Titan 80-300 HB operating at 200 kV.

PXRD. Powder X-ray diffraction (PXRD) patterns were recorded on a Bruker D2 Phaser diffractometer (Cu Kα radiation). All the samples were prepared by drying a few drops of the WS_2 dispersion on a low-background silicon sample cup.

Vis-NIR. Visible near-infrared (NIR) absorption spectra of the WS_2 dispersions in hexane were recorded using a PerkinElmer Lambda 900 spectrometer.

XPS. X-ray photoelectron spectroscopy (XPS) was performed in an ultrahigh-vacuum chamber with base pressure of 10^{-9} Torr. The system is a PerkinElmer Phi 5500 ESCA spectrometer with an Al Kα X-ray source generating X-ray photons of 1486.7 eV in energy. The spectra were obtained with an analyzer pass-energy of 23.5 eV and a scan speed of 0.05 eV s^{-1}. The samples for XPS analysis were prepared by spin coating the samples onto p-doped Si(100). All data analyses were carried out using the Multipak fitting program. The binding energies were referenced to the NIST-XPS database.

Photoactivity Evaluation. All photocatalytic tests were performed in a home-built, airtight quartz reactor. The photocatalyst powder (200 mg L^{-1}) was dispersed in distilled water and methanol (25 vol %, HPLC grade). Prior to each run the reactor was purged with nitrogen for 20 min, and a reference sample was taken before the photocatalytic reaction was started. A Newport 120 or 300 W Xe lamp was used for solar irradiation with an AM 1.5 filter (Newport). Gas samples were extracted with an airtight syringe, separated by gas chromatography (GC, Agilent 7820A GC), and detected by a thermal conductivity detector (TCD). A 1.5m Molesieve 13X column (80−100 mesh) was used for the separation of H_2, O_2, and N_2, while an integrated 1m Haysep Q column (80−100 mesh) was used to first separate CO_2 and H_2O vapors to avoid contamination of the Molesieve column.

RESULTS AND DISCUSSION

In a typical synthesis oleylamine is used as a high-boiling point coordinating solvent, as seen in other colloidal TMDC synthesis reports.[35,36] The tungsten precursor is tungsten(VI) chloride partially coordinated by oleic acid introduced in a stoichiometric amount with respect to chloride ions during the preparation of the injection mixture. The different color changes that ensue indicate alterations in the coordination sphere of the tungsten hexachloride. After the introduction of a large excess of carbon disulfide (CS_2) used as the sulfide precursor, the mixture thickens to a degree, while still allowing for syringe pump injection. During the injection of the precursor mixture at high temperature (320 °C), the solution phase turns rapidly to black, indicating the successful formation of WS_2 structures. The mode of reaction can be described as follows: (1) formation of an oleylammonium dithiocarbamate (either at room temperature or during injection); (2) thermal decomposition of the dithiocarbamate leading to an oleylammonium sulfide precursor;[21,37] (3) reduction of tungsten(VI) to tungsten(IV) by the excess sulfide; and (4) reaction of the tungsten(IV) with the sulfide ions to form WS_2. After centrifugation and redispersion in hexane, the nanostructures are colloidally stable but tend to partially aggregate over time. It is worth noting that additional washing steps by precipitation render the product less redispersible in hexane.

When observed by TEM (Figure 1a), the synthesized nanostructures present a monodisperse round-shaped sheet morphology with a mean diameter of about 100 nm. The homogeneous contrast of the nanosheets suggests they are monolayers. To further confirm the monolayer thickness of the sheets and to determine their degree of crystallinity, the sample was imaged using a HRSTEM-HAADF electron microscope (see Figures 1b and S1), revealing that the sheets are indeed monolayers but notably defected in parts. In particular, they are permeated by subnanometer voids and present some aggregates on the surface. Their monolayer nature is visible due to the

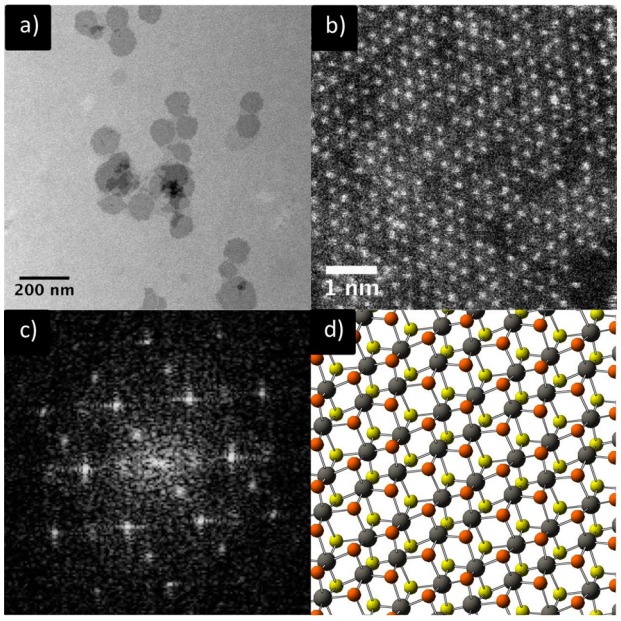

Figure 1. (a) Low-magnification TEM image of 1T-WS_2 nanosheets. (b) HAADF-HRSTEM image of a 1T-WS_2 monolayer, showing the zigzag pattern of the tungsten atoms characteristic of the distorted 1T structure as well as numerous voids and tungsten vacancies. (c) FFT of image (b). (d) Top view of a 1T-WS_2 monolayer. Tungsten atoms are in gray and sulfur atoms are in orange and yellow for top and bottom layers, respectively.

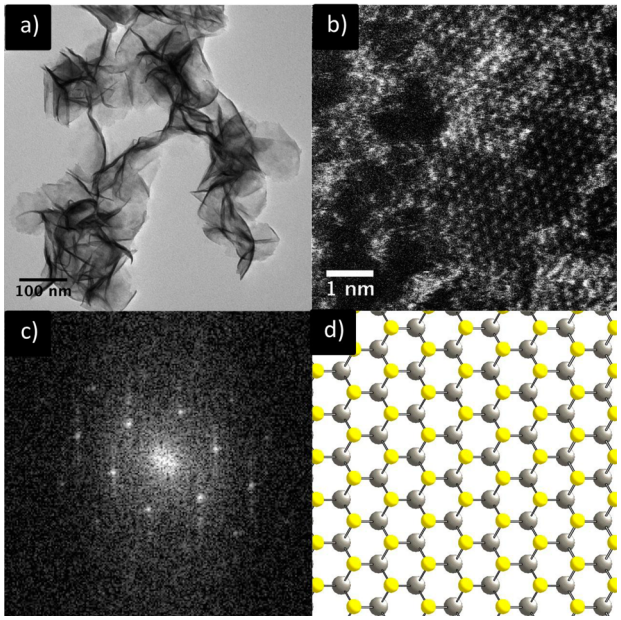

Figure 2. (a) Low-magnification TEM image of 2H-WS_2 nanostructures. (b) HAADF-HRSTEM image of a 2H-WS_2 monolayer found near the edge of the aggregates. (c) FFT of image (b). (d) Top view of a 2H-WS_2 monolayer. Tungsten and sulfur atoms are in gray and yellow, respectively.

numerous holes in the structure showing only the amorphous carbon layer beneath. It is even possible to distinguish isolated W atoms near the edges, given a contrast reference for the monolayer.

The HAADF-STEM picture in the Figure S2 shows an aggregate of 1T-WS2 nanosheets standing on an edge, clearly demonstrating that the layers are indeed made up of WS_2 monolayers only. The mean distance between them is about 2 nm, corresponding to a double layer of organic ligands.

Surprisingly, the crystal structure of the sheets (Figure 1b) is not the hexagonal packing usually observed for 2H-WS_2 but rather corresponds to a distorted 1T structure,[30] as highlighted by the fast Fourier transform (FFT, Figure 1c) of the high-resolution image. This structure is generally observed when WS_2 monolayers are prepared by lithium exfoliation. Different structures have been proposed for the Li exfoliated WS_2 and MoS_2 phases;[38−40] recent studies show that different octahedral coordination structures can be found, depending on the amount of lithium intercalated and the electron charging density of the sheets.[41,42]

After lithium exfoliation, the sheets possess a charged structure: $[WS_2]^{x-}Li^+_x$. In our case, the obtained structure is similar to ReS_2, which exhibits a distorted 1T crystal structure in the bulk phase[43] (illustrated in Figure 1d).

Through a slight modification of the synthesis, inspired by the work of Schaak et al. on the preparation of GeS and GeSe nanocrystals,[44] it is possible to obtain the hexagonal 2H-WS_2 polymorph. The addition of a small amount of HMDS, introduced either directly to the reaction flask prior to injection or into the syringe, leads to a drastic change in the morphology and crystal structure of the synthesized nanostructures. The low-magnification TEM image (Figure 2a) shows flower-like partially aggregated nanosheets. Again, HRSTEM-HAADF imaging provides the opportunity to characterize the crystal structure (Figure 2b), as it is possible to find monolayers located at the edges of the aggregates. The FFT (Figure 2c) of the monolayer reveals that indeed the expected hexagonal structure (Figure 2d) characteristic of the 2H-WS_2 polymorph is obtained.

The properties for 2H-WS_2 and 1T-WS_2 monolayers are very different. The 2H-WS_2 monolayers are semiconducting with a direct band gap of about 2 eV,[8] whereas the distorted 1T-WS_2 possess a metallic character.[45] This difference is easily highlighted by the optical properties of the two samples (Figure 3).

After dilution, the 1T-WS_2 sample appears gray, while the 2H-WS_2 sample is brown-yellow (Figure 3, inset). More precisely, the 1T-WS_2 dispersion efficiently absorbs light in the full spectral range (350−1200 nm), with a monotonic decrease of the absorbance with increasing wavelength (Figure 3, black curve). Both behaviors are characteristic of a nonplasmonic metallic nanostructure. By contrast, the 2H-WS_2 dispersion exhibits semiconducting behavior with a strong increase in absorption at lower wavelengths. The presence of excitonic features with a first peak at 607 nm and a second one around 520 nm corresponding to transitions A and B as labeled by Yoffe et al.[46] Excitons A and B correspond to direct gap transitions at the K point in the Brillouin zone.[47] The peak at 437 nm, labeled transition C in the Yoffe study, results from density of states peaks existing between valence and conduction bands.[47,48] A slight blue shift of the excitonic features A and B is observed, which are reported to be at 619 and 520 nm, respectively, for exfoliated WS_2 monolayers on a quartz substrate. Furthermore, the excitonic features are broad compared to the absorption spectrum of an exfoliated WS_2. This broadening can arise from the coupling between sheets[49] (red shift), the low crystallinity of the sample inducing quantum confinement effect within one layer[50] (blue shift),

dx.doi.org/10.1021/ja506261t | J. Am. Chem. Soc. 2014, 136, 14121−14127

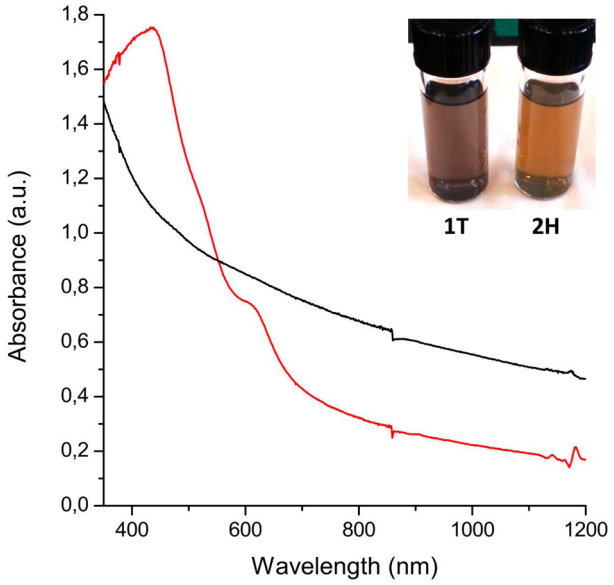

Figure 3. Absorbance spectra for colloidal solutions of 1T-WS_2 (black) and 2H-WS_2 nanosheets (red). Inset: photograph of 1T-WS_2 and 2H-WS_2 colloidal dispersions (left and right, respectively).

or from the stress experienced by the folding of sheets, which is known to have a strong effect over the value of the band gap.[51]

A second way to distinguish 1T-WS_2 and 2H-WS_2 is by XPS (Figure 4). The tungsten signal is sensitive to its oxidation state

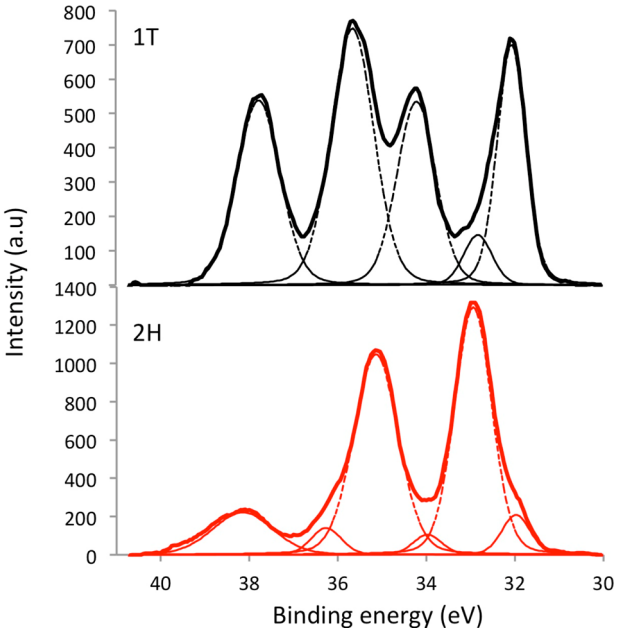

Figure 4. XPS spectra of 1T-WS_2 nanosheets (black) and 2H-WS_2 nanostructures (red) for the W4f core level peaks.

and coordination geometry, thus monitoring the position of the binding energy of the $W4f_{7/2}$ and $W4f_{5/2}$ core level peaks allows one to unambiguously distinguish between the 1T and 2H structures and can be used to observe the 1T to 2H transition.[30]

In our case, we can see that the 2H-WS_2 sample (Figure 4, red curve, and Table S1 for the assignment of the different XPS tungsten signals) characterized by tungsten peaks at 33 ev and 35 eV still contains a small amount of 1T-WS_2 (signals at 32 ev and 34 eV), as evidenced by the visible shoulder at lower binding energies. On the other hand, the 1T-WS_2 nanosheets (Figure 4, black curve) also contain a small amount of 2H-WS_2 polymorph and are partially oxidized, as evidenced by the signals at 35.75 ev and 37.9 eV. This oxidation can explain the damaged morphology of the nanosheets as seen in the HRSTEM-HAADF images (Figures 1 and S1) and the presence of some amorphous WO_3-like clusters on the surface of the nanosheets. These WO_3 clusters can be formed during the synthesis by condensation of oleylamine and oleic acid, generating water *in situ* through amide bond formation. The adventitious water can then either react with W(VI) precursors to generate WO_3 clusters[52] or directly oxidize the 1T-WS_2 nanosheets, inducing the formation of WO_3 clusters and defects on the sheets.

It is challenging to use PXRD to characterize the 1T-WS_2 and 2H-WS_2 nanostructures. The 2H-WS_2 sample is sufficiently crystalline to exhibit well-resolved diffraction peaks (Figure 5c)

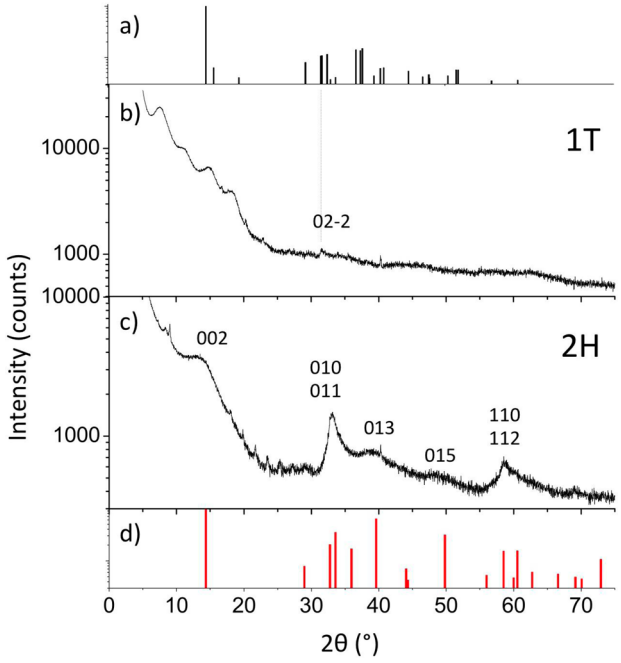

Figure 5. Powder X-ray diffractograms of 1T-WS_2 nanosheets (b) and 2H-WS_2 nanostructures (c). Bulk diffraction peaks of 2H-WS_2 (d) and calculated bulk diffraction peaks for a hypothetical distorted 1T-WS_2 with the ReS_2 structure (a).

corresponding to the known 2H-WS_2 pattern (Figure 5d). The presence of a peak at 14° corresponding to the (002) reflection indicates that the nanostructures contain WS_2 multilayers. Furthermore, the relative intensity and sharpness of the (010) and (110) peaks confirms the highly anisotropic structure of the sample. On the other hand, the 1T-WS_2 sample does not exhibit a well-defined structure (Figure 5b). We can observe a series of oscillations at low angles, characteristic of a lamellar system. Here, the mean interlayer distance is 2.4 nm, which is confirmed by HRSTEM observation (Figure S2), and can arise from 1T-WS_2 monolayers stabilized by oleylammonium ligands. For the analysis of the crystal structure, we face multiple difficulties: the low crystallinity of the sample, the presence of organic ligands, and the absence of an indexed structure for this distorted 1T-WS_2 system. To overcome this problem, we simulated a PXRD pattern using the reported ReS_2 structure[43]

dx.doi.org/10.1021/ja506261t | J. Am. Chem. Soc. 2014, 136, 14121−14127

with the lattice parameters extracted from the HRSTEM images (Figure 1b, see Supporting Information for the detailed crystal structure) and obtained the pattern shown in Figure 5a. The only slightly distinguishable peak in the experimental diffractogram (Figure 5b) corresponds to an in-plane (02-2) reflection, the axis perpendicular to the sheets corresponds to the *a*-axis for the 1T-WS_2 structure (see SI for details). To identify 1T-WS_2 or 2H-WS_2 nanosheets using a powder X-ray diffractogram, we can then resought to the peaks in the 32° region: a peak at 31.8° corresponds to the (02-2) reflection of the 1T-WS_2 structure and a peak at 32.8° corresponds to the (010) reflection of the 2H-WS_2 structure. With both reflections being purely in plane, they are suitable for the crystal structure identification of monolayers.

Using TEM, XPS, and PXRD we can then explore the conditions leading preferentially to 1T-WS_2 or 2H-WS_2 nanostructures. First of all, as the distorted octahedral (1T) structure for WS_2 is not the most thermodynamically stable one, it should be possible to induce a 1T to 2H transition by annealing at high temperature. For lithium exfoliated WS_2 samples on a substrate, the transition is reported to begin at temperatures as low as 200 °C,[30] far below the reaction temperature for this colloidal synthesis. When we anneal the reaction mixture for 30 min at 330 °C after injection, we observe a strong aggregation of the sheets and an almost complete transformation from the 1T phase to the 2H one (Supporting Information, part III).

Our first motivation to use HMDS was to reproduce the observations of Shaak et al. that shows using HMDS is necessary to obtain crystalline GeS and GeSe nanostructures.[44] However, no mechanism was proposed to explain the HMDS action. In our case we made two hypotheses: First, that HMDS can react easily with the oleate ligands complexing with the tungsten ion, activating the tungsten disulfide formation reaction. Second, HMDS can act as a ligand during the growth reaction, stabilizing the 2H-WS_2 structure over the 1T-WS_2. The first hypothesis implies that the absence of oleic acid to complex and deactivate the tungsten precursor should lead to the formation of 2H-WS_2 nanostructures. The protocol and results of the synthesis without oleic acid are summarized in the Supporting Information (part IV). These show that without oleic acid, the synthesis leads to nanosheets exhibiting a mixed 1T/2H-WS_2 phase, supporting the hypothesis that a strong coordinating ligand for the tungsten leads preferentially to 1T-WS_2. To further demonstrate this point, we perform the WS_2 synthesis with dodecanethiol (DDT) instead of oleic acid as a strong coordinated ligand. This time, as summarized in the Supporting Information (part V), we obtain pure 1T-WS_2 nanosheets. Additionally, this DDT protocol prevents the formation of WO_3 species as evidenced in the XPS spectrum. The second hypothesis, namely that HMDS acts as a ligand driving the reaction toward the 2H structure, can then be tested using the DDT protocol. As the HMDS does not react with the DDT, we will be able to observe solely the ligand effect and not the activation effect. In this case, we maintain the 1T structure, but the sheets are strongly aggregated together (see Supporting Information, part VI, for details). We can then conclude that the 1T/2H polymorphism observed for this colloidal synthesis of WS_2 is driven by the reactivity of the tungsten precursor. Low reactivity for the tungsten precursor leads to the formation of the 1T structure, whereas higher reactivity leads to the formation of the 2H structure. Tables S1 and S2 present the tungsten peak positions obtained after deconvolution as well as the relative molar percentages of 1T-WS_2, 2H-WS_2, and tungsten oxide species obtained by integration of the XPS $W4f_{7/2}$ peak for the five synthesized WS_2 compounds discussed in the text and summarize the results presented above.

In every synthesis described herein, 1T-WS_2 nanosheets are colloidally stable, whereas 2H-WS_2 nanostructures are either made of multilayers or exhibit a strong aggregation. This difference in behavior can best be explained in terms of surface charge and ligand interactions with the nanosheets. We hypothesize that in the synthetic conditions used, the distorted 1T-WS_2 structure arises from a charged $[WS_2]^-$ species, implying that the negatively charged nanosheets[39] are stabilized with oleylammonium ligands bound strongly to the surface by electrostatic interactions. The 1T-WS_2 nanosheet is then comprised of a negatively charged WS_2^- layer stabilized on either side by a positively charged oleylammonium layer. This structure at the same time prevents the aggregation and thickness growth of the nanosheets. On the other hand, the 2H-WS_2 nanosheets are considered to be neutral and coordinated weakly with the oleylamine ligands. This weak interaction between the nanosheet and ligands facilitates nucleation and growth on top of existing nanosheets, inducing the flower-like morphology during synthesis, and does not prevent aggregation. During the annealing step that transforms 1T-WS_2 to 2H-WS_2, the ligand interaction with the sheets decreases and leads to the aggregation of the 2H nanostructures. Decoupling the synthesis of the 1T-WS_2 nanosheets and their transformation into 2H-WS_2 could allow us to choose more suitable ligands and solvents to prevent aggregation and prepare colloidally stable 2H-WS_2 monolayers.

The ability to prepare the metastable 1T-WS_2 nanosheets at temperatures higher than the 1T to 2H transition temperature is rather surprising. However, it is well-known in colloidal quantum dot syntheses that the crystal phase can be governed by the surface ligands more than the reaction temperature. For example, there is a zinc-blende/wurtzite polytypism in CdSe colloidal nanocrystals, allowing for the formation of pure zinc-blende or pure wurtzite nanocrystals depending on the ligands used.[53,54] Such syntheses usually occur between 240 and 330 °C, but the zinc-blende to wurtzite crystal structure transition can occur at much lower temperatures. In colloidal nanocrystal systems, the ligand interactions with the surface can then stabilize a metastable crystal structure and prevent its transition to the thermodynamically stable one.

In addition to the synthesis and characterization, we aim to compare the photocatalytic activity of the semiconducting and metallic WS_2 nanostructures. We use P25-TiO_2 nanopowder as the platform to create nanocomposite TiO_2-WS_2 as a model water splitting photosystem. By a simple adsorption protocol, we obtain TiO_2 powders loaded either with 1T-WS_2 nanosheets or with 2H-WS_2 nanostructures. As the distorted 1T-WS_2 nanosheets are reported to function as an efficient electrocatalyst,[30] we expect that these nanosheets can also act as a hydrogen evolution cocatalyst when associated with a suitable light absorber, namely TiO_2. In this case, after absorption of a photon, the photogenerated electron will be quickly transferred to the 1T-WS_2 to perform proton reduction in aqueous solution. Supporting this proposal, the XPS measurements performed on the 1T-WS_2 sample indicate a high work function of ∼4.2 eV, facilitating the proton reduction reaction. On the other hand, as the 2H-WS_2 nanostructures are semiconducting, they can act as an efficient light harvesting material, transferring the photogenerated electron to TiO_2 after absorption of a

dx.doi.org/10.1021/ja506261t | J. Am. Chem. Soc. 2014, 136, 14121−14127

photon. A sketch of the experimentally determined electronic band alignment between TiO_2, 1T-WS_2 and 2H-WS_2 is displayed Figure 6a.

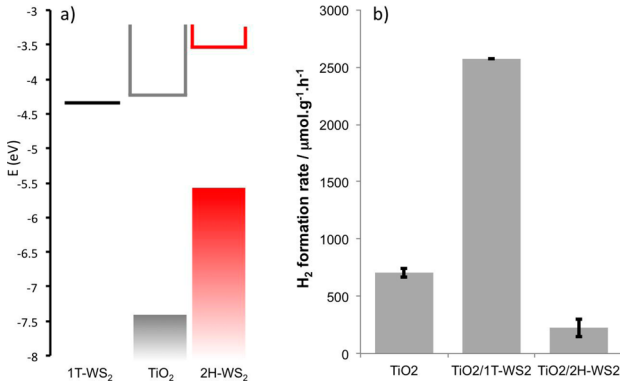

Figure 6. (a) Electronic band alignment between TiO_2 and synthesized 1T-WS_2 and 2H-WS_2 nanostructures. (b) Photocatalytic hydrogen production rates for P25-TiO_2 and the TiO_2:1T-WS_2 and TiO_2:2H-WS_2 nanocomposites.

Under illumination with a 300 W Xe source with an AM 1.5 filter, a P25-TiO_2 dispersion in a mixture of water and methanol (3:1 in volume, acting as a hole scavenger) produces hydrogen gas at a rate of 700 μmol g^{-1} h^{-1} (Figure 6b). When integrated with the synthesized 1T-WS_2 nanosheets, the rate increases by more than 3-fold to 2570 μmol g^{-1} h^{-1} at an optimized loading of 1% weight (see Figure S11). This significant increase of photoactivity clearly demonstrates the role of the distorted metallic 1T-WS_2 nanosheets as an effective cocatalyst for H_2 evolution. The hydrogen evolution reaction is stable under these conditions for more than 20 h (Figure S12). On the other hand, the same P25-TiO_2 powder combined with the semiconducting 2H-WS_2 nanostructure causes the hydrogen evolution rate to instead decrease to 225 μmol g^{-1} h^{-1}. In this case, the presence of semiconducting 2H-WS_2 layers introduces efficient recombination centers for the electrons and holes photogenerated in the TiO_2 and causes the photocatalytic activity to diminish by more than a factor of 3. The low rates observed could also result from the multilayer structure of the 2H-WS_2 sample, which hinders the charge injection into TiO_2.[55] We note that even if the global activity of the catalyst strongly decreases after combination with 2H-WS_2, the TMDC nanostructure still can act as a visible light sensitizer. Upon visible light illumination only (using a 495 nm cutoff filter to avoid any TiO_2 light absorption), the catalyst is still active and produces hydrogen at 5 μmol g^{-1} h^{-1} (Figure S13). As expected, the TiO_2:1T-WS_2 nanocomposite does not show any photoactivity under visible light.

CONCLUSION

We have developed a colloidal synthesis method for preparing metallic distorted 1T-WS_2 monolayer nanosheets. By slight modifications of the synthesis protocol, we highlight the possibility of obtaining semiconducting 2H-WS_2 nanosheets but at the expense of their monolayer thickness. The ability to obtain one structure or the other is controlled by the reactivity of the tungsten precursor and the reaction time. The distorted 1T-WS_2 structure is demonstrated to be an efficient hydrogen evolution cocatalyst, whereas the 2H-WS_2 structure can act as a visible light sensitizer. Furthermore, TiO_2:2H-WS_2 nanocomposite exhibits low photoactivity induced by the electron−hole recombination centers it provides.

The colloidal synthesis developed here allows for the formation of colloidally stable monodisperse round-shaped 1T-WS_2 monolayers. This is in strong contrast with the alternative method to prepare 1T-WS_2 by lithium exfoliation, which produces polydisperse irregular shaped monolayers. Furthermore, the mean size of the synthesized 1T-WS_2 monolayers is 1 order of magnitude smaller than the nanosheets obtained by exfoliation, which is advantageous for the integration of these materials as cocatalysts, for example, in photochemical hydrogen production systems.

The colloidal synthesis of the distorted 1T-WS_2 structure can be an efficient strategy to produce large quantities of monolayer TMDC, as the stabilization of such layers is more efficient and prevents both further thickness growth and aggregation. The possibility to extend this approach to other TMDCs like WSe_2 and MoS_2 as well as preparing integrated nanosheet systems is currently under investigation. One can imagine preparing 1T-TMDC monolayers, depositing them on a substrate and then annealing them to induce the formation of the 2H monolayers. This approach can open the door to doping and alloying and to the creation of monolayered heteronanostructures of either the 1T or 2H type. The herein reported control of the structure during the synthesis between a semiconducting and a metallic phase can also provide an opportunity to develop colloidal semiconducting metallic heteronanostructures made of the same material, such as 2H-WS_2:1T-WS_2.[56]

ASSOCIATED CONTENT

Supporting Information

Additional STEM images of 1T-WS_2 nanosheets, crystal structure of the distorted 1T-WS_2, annealing effect on 1T-WS_2 nanosheets, additional syntheses and photocatalysis experiments. This material is available free of charge via the Internet at http://pubs.acs.org.

AUTHOR INFORMATION

Corresponding Author

gozin@chem.utoronto.ca

Notes

The authors declare no competing financial interest.

ACKNOWLEDGMENTS

G.A.O. is Government of Canada Research Chair in Materials Chemistry and Nanochemistry. We are deeply indebted to the Ontario Ministry of Research and Innovation (MRI), the Ontario Ministry of Economic Development and Innovation (MEDI), the Natural Sciences and Engineering Council of Canada (NSERC), and the University of Toronto for strong and sustained support of our solar fuels research. We also appreciate the support of the Canadian Center for Electron Microscopy at McMaster University and University of Texas at San Antonio, which enabled high-resolution imaging of the 2H-WS_2 and 1T-WS_2 nanosheets, respectively.

REFERENCES

(1) Novoselov, K. S.; Jiang, D.; Schedin, F.; Booth, T. J.; Khotkevich, V. V.; Morozov, S. V.; Geim, a K. *Proc. Natl. Acad. Sci. U. S. A.* **2005**, *102*, 10451.

(2) Hernandez, Y.; Nicolosi, V.; Lotya, M.; Blighe, F. M.; Sun, Z.; De, S.; McGovern, I. T.; Holland, B.; Byrne, M.; Gun'Ko, Y. K.; Boland, J. J.; Niraj, P.; Duesberg, G.; Krishnamurthy, S.; Goodhue, R.;

Hutchison, J.; Scardaci, V.; Ferrari, A. C.; Coleman, J. N. *Nat. Nanotechnol.* **2008**, *3*, 563.
(3) Li, X.; Cai, W.; An, J.; Kim, S.; Nah, J.; Yang, D.; Piner, R.; Velamakanni, A.; Jung, I.; Tutuc, E.; Banerjee, S. K.; Colombo, L.; Ruoff, R. S. *Science* **2009**, *324*, 1312.
(4) Liu, R.; Wu, D.; Feng, X.; Müllen, K. *J. Am. Chem. Soc.* **2011**, *133*, 15221.
(5) Xu, M.; Liang, T.; Shi, M.; Chen, H. *Chem. Rev.* **2013**, *113*, 3766.
(6) Nicolosi, V.; Chhowalla, M.; Kanatzidis, M. G.; Strano, M. S.; Coleman, J. N. *Science* **2013**, *340*, 1226419.
(7) Chhowalla, M.; Shin, H. S.; Eda, G.; Li, L.-J.; Loh, K. P.; Zhang, H. *Nat. Chem.* **2013**, *5*, 263.
(8) Wang, Q. H.; Kalantar-Zadeh, K.; Kis, A.; Coleman, J. N.; Strano, M. S. *Nat. Nanotechnol.* **2012**, *7*, 699.
(9) Jaramillo, T. F.; Jørgensen, K. P.; Bonde, J.; Nielsen, J. H.; Horch, S.; Chorkendorff, I. *Science* **2007**, *317*, 100.
(10) Bernardi, M.; Palummo, M.; Grossman, J. C. *Nano Lett.* **2013**, *13*, 3664.
(11) Gu, X.; Cui, W.; Li, H.; Wu, Z.; Zeng, Z.; Lee, S.-T.; Zhang, H.; Sun, B. *Adv. Energy Mater.* **2013**, *3*, 1262.
(12) Jariwala, D.; Sangwan, V. K.; Lauhon, L. J.; Marks, T. J.; Hersam, M. C. *ACS Nano* **2014**, *8*, 1102.
(13) Yin, Z.; Li, H.; Li, H.; Jiang, L.; Shi, Y.; Sun, Y.; Lu, G.; Zhang, Q.; Chen, X.; Zhang, H. *ACS Nano* **2012**, *6*, 74.
(14) Zhu, B.; Zeng, H.; Dai, J.; Cui, X. *Adv. Mater.* **2014**, *26*, 5504.
(15) Ayari, A.; Cobas, E.; Ogundadegbe, O.; Fuhrer, M. S. *J. Appl. Phys.* **2007**, *101*, 014507.
(16) Coleman, J. N.; Lotya, M.; O'Neill, A.; Bergin, S. D.; King, P. J.; Khan, U.; Young, K.; Gaucher, A.; De, S.; Smith, R. J.; Shvets, I. V.; Arora, S. K.; Stanton, G.; Kim, H.-Y.; Lee, K.; Kim, G. T.; Duesberg, G. S.; Hallam, T.; Boland, J. J.; Wang, J. J.; Donegan, J. F.; Grunlan, J. C.; Moriarty, G.; Shmeliov, A.; Nicholls, R. J.; Perkins, J. M.; Grieveson, E. M.; Theuwissen, K.; McComb, D. W.; Nellist, P. D.; Nicolosi, V. *Science* **2011**, *331*, 568.
(17) Miremadi, B. K.; Morrison, S. R. *J. Appl. Phys.* **1988**, *63*, 4970.
(18) Zeng, Z.; Yin, Z.; Huang, X.; Li, H.; He, Q.; Lu, G.; Boey, F.; Zhang, H. *Angew. Chem., Int. Ed. Engl.* **2011**, *50*, 11093.
(19) Song, J.; Park, J.; Lee, W.; Choi, T.; Jung, H.; Lee, C. W.; Hwang, S.; Myoung, J. M.; Jung, J.; Kim, S.-H.; Lansalot-Matras, C.; Kim, H. *ACS Nano* **2013**, *7*, 11333.
(20) Peimyoo, N.; Shang, J.; Cong, C.; Shen, X.; Wu, X.; Yeow, E. K. L.; Yu, T. *ACS Nano* **2013**, *7*, 10985.
(21) Seo, J.-W.; Jun, Y.-W.; Park, S.-W.; Nah, H.; Moon, T.; Park, B.; Kim, J.-G.; Kim, Y. J.; Cheon, J. *Angew. Chem., Int. Ed. Engl.* **2007**, *46*, 8828.
(22) Altavilla, C.; Sarno, M.; Ciambelli, P. *Chem. Mater.* **2011**, *23*, 3879.
(23) Antunez, P. D.; Webber, D. H.; Brutchey, R. L. *Chem. Mater.* **2013**, *25*, 2385.
(24) Park, K. H.; Choi, J.; Kim, H. J.; Oh, D.-H.; Ahn, J. R.; Son, S. U. *Small* **2008**, *4*, 945.
(25) Gutiérrez, H. R.; Perea-López, N.; Elías, A. L.; Berkdemir, A.; Wang, B.; Lv, R.; López-Urías, F.; Crespi, V. H.; Terrones, H.; Terrones, M. *Nano Lett.* **2013**, *13*, 3447.
(26) Jo, S.; Ubrig, N.; Berger, H.; Kuzmenko, A. B.; Morpurgo, A. F. *Nano Lett.* **2014**, *14*, 2019.
(27) Zong, X.; Han, J.; Ma, G.; Yan, H.; Wu, G.; Li, C. *J. Phys. Chem. C* **2011**, *115*, 12202.
(28) Wypych, F.; Schöllhorn, R. *J. Chem. Soc. Chem. Commun.* **1992**, 1386.
(29) Voiry, D.; Salehi, M.; Silva, R.; Fujita, T.; Chen, M.; Asefa, T.; Shenoy, V. B.; Eda, G.; Chhowalla, M. *Nano Lett.* **2013**, *13*, 6222.
(30) Voiry, D.; Yamaguchi, H.; Li, J.; Silva, R.; Alves, D. C. B.; Fujita, T.; Chen, M.; Asefa, T.; Shenoy, V. B.; Eda, G.; Chhowalla, M. *Nat. Mater.* **2013**, *12*, 850.
(31) Lukowski, M. A.; Daniel, A. S.; English, C. R.; Meng, F.; Forticaux, A.; Hamers, R. J.; Jin, S. *Energy Environ. Sci.* **2014**, *7*, 2608.
(32) Lukowski, M. a.; Daniel, A. S.; Meng, F.; Forticaux, A.; Li, L.; Jin, S. *J. Am. Chem. Soc.* **2013**, *135*, 10274.
(33) Ran, J.; Zhang, J.; Yu, J.; Jaroniec, M.; Qiao, S. Z. *Chem. Soc. Rev.* **2014**, advance article.
(34) Ding, Q.; Meng, F.; English, C. R.; Cabán-Acevedo, M.; Shearer, M. J.; Liang, D.; Daniel, A. S.; Hamers, R. J.; Jin, S. *J. Am. Chem. Soc.* **2014**, *136*, 8504.
(35) Plashnitsa, V. V.; Vietmeyer, F.; Petchsang, N.; Tongying, P.; Kosel, T. H.; Kuno, M. *J. Phys. Chem. Lett.* **2012**, *3*, 1554.
(36) Jeong, S.; Yoo, D.; Jang, J.-T.; Kim, M.; Cheon, J. *J. Am. Chem. Soc.* **2012**, *134*, 18233.
(37) Jung, Y. K.; Kim, J. Il; Lee, J.-K. *J. Am. Chem. Soc.* **2010**, *132*, 178.
(38) Wypych, F.; Weber, T.; Prins, R. *Chem. Mater.* **1998**, *10*, 723.
(39) Wypych, F.; Sollmann, K.; Schöllhorn, R. *Mater. Res. Bull.* **1992**, *27*, 545.
(40) Heising, J.; Kanatzidis, M. G. *J. Am. Chem. Soc.* **1999**, *121*, 638.
(41) Kan, M.; Wang, J. Y.; Li, X. W.; Zhang, S. H.; Li, Y. W.; Kawazoe, Y.; Sun, Q.; Jena, P. *J. Phys. Chem. C* **2014**, *118*, 1515.
(42) Wang, L.; Xu, Z.; Wang, W.; Bai, X. *J. Am. Chem. Soc.* **2014**, *136*, 6693.
(43) Murray, H. H.; Kelty, S. P.; Chianelli, R. R.; Day, C. S.; Company, C. *Inorg. Chem.* **1994**, *33*, 4418.
(44) Vaughn, D. D.; Patel, R. J.; Hickner, M. A.; Schaak, R. E. *J. Am. Chem. Soc.* **2010**, *132*, 15170.
(45) Bissessur, R.; Kanatzidis, M. G.; Schindler, J. L.; Kannewurf, C. R. *J. Chem. Soc. Chem. Commun.* **1993**, 1582.
(46) Wilson, J.; Yoffe, A. *Adv. Phys.* **1969**, *18*, 193.
(47) Zhao, W.; Ghorannevis, Z.; Chu, L.; Toh, M.; Kloc, C.; Tan, P.-H.; Eda, G. *ACS Nano* **2013**, *7*, 791.
(48) Mattheiss, L. *Phys. Rev. B* **1973**, *8*, 3719.
(49) Zhao, W.; Ribeiro, R. M.; Toh, M.; Carvalho, A.; Kloc, C.; Castro Neto, a H.; Eda, G. *Nano Lett.* **2013**, *13*, 5627.
(50) Chikan, V.; Kelley, D. *J. Phys. Chem. B* **2002**, 3794.
(51) Yun, W. S.; Han, S. W.; Hong, S. C.; Kim, I. G.; Lee, J. D. *Phys. Rev. B* **2012**, *85*, 033305.
(52) Seo, J.-W.; Jun, Y.-W.; Ko, S. J.; Cheon, J. *J. Phys. Chem. B* **2005**, *109*, 5389.
(53) Mahler, B.; Lequeux, N.; Dubertret, B. *J. Am. Chem. Soc.* **2010**, *132*, 953.
(54) Gao, Y.; Peng, X. *J. Am. Chem. Soc.* **2014**, *136*, 6724.
(55) Yu, Y.; Huang, S.-Y.; Li, Y.; Steinmann, S. N.; Yang, W.; Cao, L. *Nano Lett.* **2014**, *14*, 553.
(56) Eda, G.; Fujita, T.; Yamaguchi, H.; Voiry, D.; Chen, M.; Chhowalla, M. *ACS Nano* **2012**, *6*, 7311.